Renewable Energy 172 (2021) 1133–1144

Contents lists available at ScienceDirect

Renewable Energy

journal homepage: www.elsevier.com/locate/renene

Unbalanced sediment transport by tidal power generation in Lake Sihwa

J.W. Kim [a], H.K. Ha [a, *], S.-B. Woo [a], M.-S. Kim [a], H.-K. Kwon [b]

[a] Department of Ocean Sciences, Inha University, Incheon, 22212, Republic of Korea
[b] Korea Water Resources Corporation, Ansan, 15637, Republic of Korea

ARTICLE INFO

Article history:
Received 16 August 2020
Received in revised form
5 February 2021
Accepted 18 March 2021
Available online 23 March 2021

Keywords:
Discharge
Residual sediment flux
Sihwa tidal power plant
Sediment accumulation

ABSTRACT

An in-situ observational study was conducted to understand the sediment transport processes disturbed by the flood generation type of Sihwa tidal power plant (TPP). A surface mooring was deployed in Lake Sihwa (inside of TPP) to collect time-series data of the current velocity and suspended sediment concentration (SSC). A TPP with a capacity of 254 MW has four sequential phases (power generation −standby−drain−standby) of operation. The SSC during power generation was one order of magnitude higher than that during drain, which led to heavily unbalanced sediment fluxes. The total residual sediment flux was always negative (into the lake), which was attributed to the mean advection processes associated with the discharge. Over 18 day mooring period, 78.28 tons m^{-1} of sediment was delivered to the lake. The source of delivered sediment might be attributed to more local resuspension than the sediment inflow through the gates of TPP. Since the maximum sediment influx during power generation occurred within the water head difference of 4–6 m, the reduction in discharge rate can be a possible measure for solving the sediment accumulation within Lake Sihwa.

© 2021 Elsevier Ltd. All rights reserved.

1. Introduction

Understanding sediment transport in a coastal region is important in many aspects including the benthic ecology, biogeochemistry, and marine geology [1,2]. With increasing coastal development, sediment transport is being influenced by not only natural processes but also anthropogenic disturbances. In typical estuarine systems, sediment transport is controlled by many natural factors, such as river discharge, tidal characteristics, and sediment composition [3,4]. In an estuary disturbed by artificial activities, however, human behavior has a significant influence on sediment transport. For example, the Lake Poyang Basin was converted from a deposition-dominant to an erosion-dominant system due to the increase in total sediment outflux associated with sand mining [5]. In Hillsborough Bay on the west-central coast of Florida, the sediment transport derived from vessel-generated solitary long waves along a dredged ship channel was one order of magnitude greater than that from winter storms [6].

A tidal power plant (TPP) is a marine infrastructure built for electricity generation using the potential energy of tides [7]. The TPP consists of hydraulic turbines and sluice gates controlled by artificial activities. The operation methods can be categorized into three types [8]: ebb generation, flood generation, and two-way generation. Because of the advantages of a renewable energy resource, numerous TPPs have been constructed in many coastal regions, and their operations have had a socio-economic benefit [7,9–11]. However, the operation of TPPs has changed the sedimentary processes due to decrease in tidal forcing [12,13]. In the eastern Irish Sea, the intertidal zones were expected to be reduced after the construction of a two-way generation TPP [14]. In the Severn Barrage system, the suspended sediment concentration (SSC) was predicted to be significantly reduced through the hypothetical numerical experiment [15]. Understanding these dramatic changes in sedimentary processes caused by the operation of a TPP is important because they are linked dynamically to the geomorphology, ecology, and water quality [16].

Changes in sedimentary processes were also observed in the Sihwa region due to the operation of the TPP, which located in the middle of the seawall, west coast of the Korean Peninsula. The mean tidal range was 5.5 m, and the capacity of turbines and generators installed in Sihwa TPP was 254 MW. During power generation phase, the discharge carried out by introducing seawater into Lake Sihwa (upstream of TPP) through the 10 gates

* Corresponding author.
E-mail addresses: hahk@inha.ac.kr, hokyung.ha@gmail.com (H.K. Ha).

https://doi.org/10.1016/j.renene.2021.03.088
0960-1481/© 2021 Elsevier Ltd. All rights reserved.

with the turbines. During drain phase, the discharge carried out by exiting the filled seawater to the sea (downstream of TPP) through the 10 gates with the turbines and 8 gates without the turbines [17]. Kim et al. [18] reported that the suspension of bed sediment was caused by the strong jet-flow (>1 m s^{-1}) during the drain phase. Considering the model results for residual flow field presented in Kim [19], the inflow of suspended sediment towards the upstream may increase with the anticlockwise rotating vortex. These disturbances of the sediment dynamics associated with the operation of Sihwa TPP have increased concerns about the sediment accumulation within the lake [20].

Despite diverse sedimentary changes since the operation of TPP, a close scientific analysis for revealing major causes of these changes has not been conducted sufficiently. In particular, a quantitative analysis has not been attempted to interpret how the sediment accumulation in the upstream could be affected by the characteristics of the flood generation type. Therefore, this study analyzed the characteristics of the hydrodynamics and sediment transport in response to the flood generation type in the upstream using field observation data. Continuous observations of the SSC were conducted together with measurements of the velocity and salinity at a mooring station (M3 in Fig. 1a), which was located 1 km upstream of TPP gates. The objectives of this study are (1) to understand the disturbance in sediment dynamics by the operation of Sihwa TPP and (2) to reveal the driving mechanisms of sediment accumulation in the upstream.

2. Study area

Lake Sihwa has an artificial seawall with a length of 12.7 km that was constructed in 1994 (Fig. 1a). The water volume is 3.23×10^8 m^3, and the surface area is about 30 km^2. The percentages of gravel, sand, silt, and clay in the seabed sediment were 0.3, 34.6, 55.1, and 10.0%, respectively [21]. Before the operation of TPP began, water pollution within the lake had accelerated due to contaminant input and stratification. For example, the increase in organic matter induced by the massive nutrient loading from industrial complexes caused oxygen depletion in the water column, resulting in hypoxia near the bed [22,23]. The restriction of vertical material mixing due to the strong stratification produced by the polluted freshwater input was the primary source of water pollution [24,25]. After the operation of the TPP began in 2011, the water quality was improved noticeably, owing to the strong mixing derived from the periodic discharge [26]. The freshwater sources are the creeks of nearby cities and industrial and agricultural complexes. The combined length of all the creeks is less than 10 km,

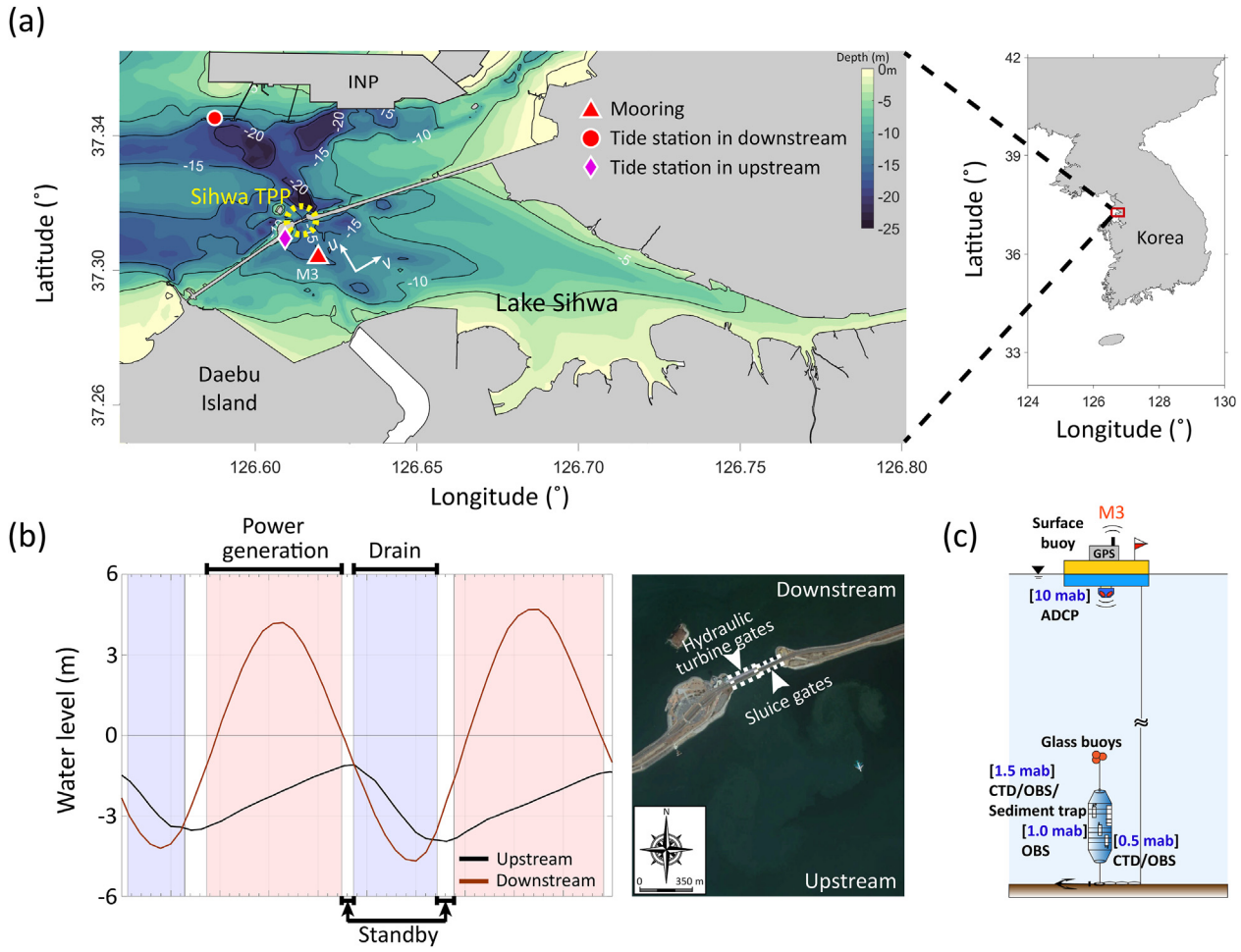


Fig. 1. (a) Map showing Lake Sihwa (upstream) and the adjacent region. The time series of the velocity, salinity, and acoustic backscatter were collected at a mooring site (red triangle, M3). The tide in the sea (downstream) was measured at the Songdo tide station (red circle). The water level in the upstream and discharge data were collected from Lake Sihwa tide station (purple diamond). Along (u)- and across (v)-channel components represent the ADCP velocities rotated by +30.25° in parallel with the axis of the discharge. INP denotes the Incheon New Port. (b) The water levels in the downstream and the upstream over the power generation cycle and satellite image near the TPP (source: Google Earth). There were two operation phases (power generation and drain) and standby phases. (c) Schematic diagram of the mooring system (M3).

and their freshwater discharge was about 3.40×10^8 m^3 yr^{-1} [27]. This freshwater discharge was very small compared to the seawater input (1.47×10^8 m^3) during one tidal power generation cycle, as reported by Bae et al. [17]. Considering the discharge ratio between seawater input through the TPP gates and freshwater input from land, the sediment inflow into the lake through the operation of TPP will be dominant.

The tide in the downstream exhibited typical semi-diurnal tides with spring-neap variations composed of four major constituents (M_2, S_2, K_1, and O_1). The mean spring and neap tidal ranges were about 7.7 m and 3.3 m, respectively. The water level in the upstream rises to −1.0 m due to seawater input during power generation, whereas that falls to −5.0 m due to seawater output during drain phase. No water exchange between the downstream and upstream occurs during the standby phase between power generation and drain.

The discharge and power output through the turbine were formulated by curve-fitting method when the Hill Chart was completed by turbine manufacturer after design and factory model test, and those were expressed as a function of water head difference (η_{diff}) by the equation presented by Bae et al. [17] (Fig. 2). The η_{diff} of at least 1 m was required to spin the turbine for Sihwa TPP. Due to the generator efficiency, the power out and discharge reached 22.29 MW and 474.4 m^3 s^{-1} at a η_{diff} of 5.64 m, respectively. At the η_{diff} above 5.64 m, the discharge steadily declined, and the power output maintained at 22.29 MW.

3. Materials and methods

3.1. Data collection

Prior to the deployment of mooring, a suitable location was evaluated to collect high-quality data directly influenced by the jet or wake of the turbines from Sihwa TPP. Similar to the Severn Barrage systems [28,29], a jet-flow was formed within 2.5 km radius of TPP during both power generation and drain phases presented by Kang et al. [30]. A surface mooring (M3) was deployed 1.06 km within the jet inward from Sihwa TPP with a mean depth of 13.1 m (Fig. 1a; 37°18′17.40"N, 126°37′5.40"E) between April 14 and May 6, 2015. The mooring system was designed to measure the near-bed temperature, salinity, and turbidity using conductivity-temperature-depth (CTD) sensors (RBR, XR-420, and Concerto) and an optical backscatter sensor (OBS) (Seapoint Turbidity Meter). Two CTDs were installed at 1.5 and 0.5 m above the bottom (mab), and three OBSs were installed at 1.5, 1.0, and 0.5 mab (Fig. 1c). Both CTDs and OBSs were recorded every 10 min.

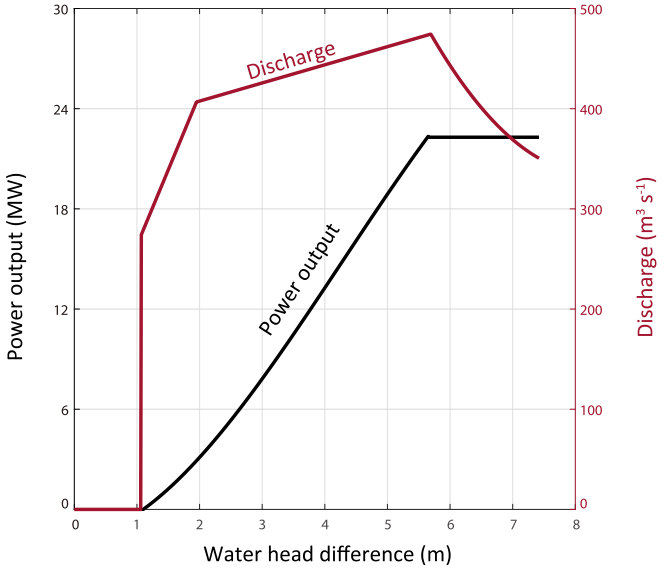


Fig. 2. Relationship between water head difference, power output and discharge for Sihwa TPP.

The velocity profiles and backscatter intensities were measured with a downward-looking acoustic Doppler current profiler (ADCP) (RDI, 600 kHz WorkHorse Sentinel). The ADCP was operated in burst mode every 30 min with an ensemble average of 60 pings and a vertical resolution of 0.25 m. Table 1 provides details of the setup and configuration of the mooring. The velocities were decomposed into along (u)- and across (v)-channel components using principal component analysis. The velocities were determined by finding the major axis rotated about +30.25° (Fig. 1a). The ADCP bins corresponding to the uppermost 0–1.5 m of the water column and below 1.0 mab were discarded from velocity data analysis because of the undesirable noise from side-lobe interference. The water levels in the downstream and upstream were measured at the Songdo and Lake Sihwa tide stations (Fig. 1a), respectively. The data for the opening and closing times of the sluice gates were obtained from the T-LIGHT station operated by the Korea Water Resources Corporation (http://tlight.kwater.or.kr).

3.2. Estimation of SSC from acoustic backscatter intensity

The water samples were collected at deployment depths of OBSs using a Niskin water sampler. To calculate the in-situ SSC ($SSC_{\text{in-situ}}$), volumes of water (0.9–1.0 l) were filtered through a pre-weighed and pre-dried GF/F (0.7 μm). The filters were oven-dried at 100 °C for 48 h and reweighed. The backscattered strengths of three OBSs were converted to the SSC (SSC_{OBS}) through the calibration against $SSC_{\text{in-situ}}$ (Fig. 3). The suspended sediments were collected by sediment traps at 1.5 mab, and median grain size (d_{50}) was 12 μm.

The SSC in the entire water column (SSC_{ADCP}) was estimated by inversion of the ADCP backscatter intensity. It was calibrated with the modified sonar equation as follows [31,32]:

$$\overline{S_v} = K_c E + C' \quad (1)$$

where $= 10 \cdot \log(SSC_{\text{OBS}}) - 2(\alpha_w + \alpha_s)R - 10 \cdot \log(R^2)$ was the net volume scattering, E was the acoustic backscatter intensity, R was the range between transducer and measurement volume, α_w and α_s were sound attenuation coefficients due to water and suspended sediment, respectively. The α_w was calculated using the salinity, temperature, and pressure data of CTD suggested by Fisher and Simmons [33]. The α_s was determined by calculating the sound absorption components that varied with grain size [34]. For

Table 1
Setup of the deployed ADCP, CTD, and OBS.

	M3
ADCP	
Bin size (m)	0.25
Sampling rate (Hz)	1
Burst interval (min)	30
Burst duration (min)	10
Deployment depth (mab)	13
Blanking distance (m)	0.50
CTD and OBS	
Sampling rate (Hz)	1
Burst interval (min)	10
Burst duration (min)	1
Deployment depths (mab)	3 levels (1.5, 1.0, and 0.5)

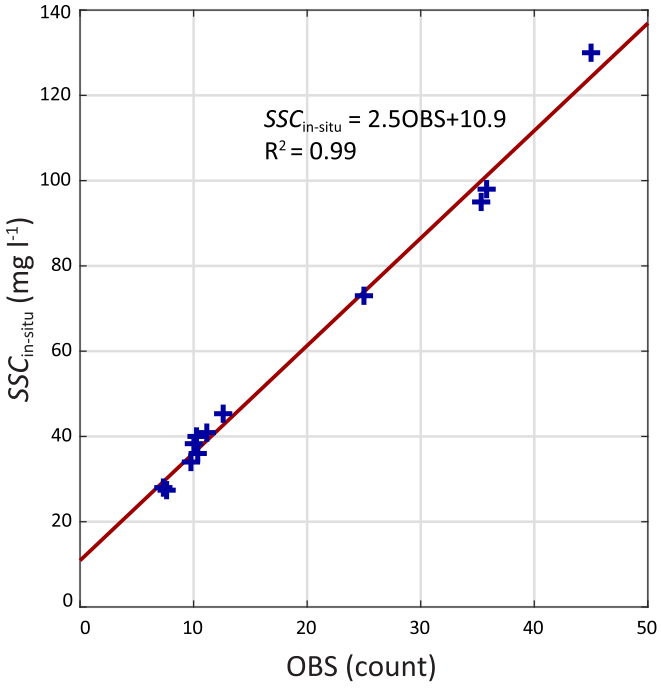


Fig. 3. Calibration of OBS with SSC derived from water samples ($SSC_{in\text{-}situ}$).

$d_{50} \approx 12$ μm and $SSC_{in\text{-}situ} = 57.2$ mg l^{-1}, α_s was negligibly small compared to α_w. The K_c and C' were the signal calibration coefficients and were obtained from linear regression ($R^2 = 0.54$ in Fig. 4), which was then used to estimate the SSC profiles at M3. The backscattered intensity of ADCP is more affected by sandy particles rather than muddy particles due to the efficient backscatter of particles associated with the emitted acoustic wavelength [32]. For this reason, the R^2 at M3 can be attributed to muddy particles ($d_{50} \approx 12$ μm). In addition, although the R^2 was 0.51–0.67, there is a case of successfully converting measured acoustic backscatters to SSC at the Han River estuary including the Sihwa region [35].

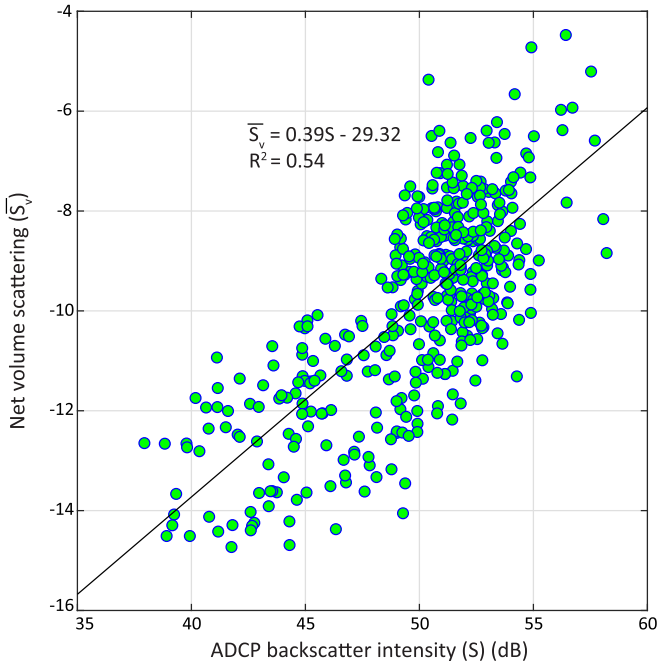


Fig. 4. Linear regression between net volume scattering and ADCP backscatter intensity.

To examine the inversion performance of acoustic backscatter intensity to SSC at M3, the mean error (ME), mean absolute error (MAE), and mean relative error (MRE) are calculated by the equations expressed as:

$$\mathrm{ME} = \frac{1}{\mathrm{N}}\sum SSC_{\mathrm{ADCP}} - SSC_{\mathrm{OBS}} \tag{2a}$$

$$\mathrm{MAE} = \frac{1}{\mathrm{N}}\sum |SSC_{\mathrm{ADCP}} - SSC_{\mathrm{OBS}}| \tag{2b}$$

$$\mathrm{MRE} = \frac{\sum |SSC_{\mathrm{ADCP}} - SSC_{\mathrm{OBS}}|}{\sum SSC_{\mathrm{OBS}}} \times 100 \tag{2c}$$

where N is the number of data. ME represents the bias of SSC_{ADCP} for SSC_{OBS}. MAE represents the absolute value of the error between SSC_{ADCP} and SSC_{OBS}. When the MAE is low, the SSC conversion was assumed to be reasonable. MRE is the percent of MAE to the mean of SSC_{OBS}. For the inversion of acoustic backscatter intensity to SSC, the estimate SSC_{ADCP} has MRE of 36.2% for SSC_{OBS}. The SSC_{ADCP} slightly underestimates the SSC_{OBS} with ME of −2.1 mg l^{-1}, and average deviation between SSC_{ADCP} and SSC_{OBS} is the MAE of 24.2 mg l^{-1}. ME, MAE, and MRE are comparable to ME of −16.8–15.7 mg l^{-1}, MAE of 50.1–51.6 mg l^{-1}, and MRE of 45–47% at Han River estuary presented in Park and Lee [35].

3.3. Sediment flux calculation and decomposition

To calculate the sediment flux, the profiles of SSC_{ADCP} and u were transformed from the z-coordinates to σ-coordinates with 21 equally spaced σ-levels, where $\sigma = z/H$; z is the depth of each bin in the ADCP and H is the time-varying total depth. The seabed and free surface are represented by $\sigma = 0$ and $\sigma = 1$, corresponding to $z = 0$ and $z = H$, respectively. This conversion is the most suitable approach to calculate the mass transport in a macrotidal estuary, where the tidal range is comparable to the mean depth [36]. The instantaneous sediment flux per unit width (F) was calculated by integrating the product of the along-channel velocity (u_σ) and SSC (SSC_σ),

$$F = H\int_0^1 u_\sigma \cdot SSC_\sigma d\sigma. \tag{3}$$

The total residual sediment flux (F_T) at M3 was obtained from the tidally averaging F. The tidal averaging procedure was accomplished using a low-pass Lanczos filter with a cut-off frequency of 48 h. The time series of F_T was decomposed into the mean advective flux (F_A) and the tidal dispersive flux (F_D) as follows [37,38]:

$$F_A = [H]\int_0^1 [u_\sigma]\cdot[SSC_\sigma]d\sigma, \tag{4a}$$

$$F_D = \left[H'\int_0^1 u_\sigma'\cdot SSC_\sigma' d\sigma\right], \tag{4b}$$

where $[u_\sigma]$, $[SSC_\sigma]$, and $[H]$ are the tidally averaged u_σ, SSC_σ, and H, respectively, and u_σ' ($=u_\sigma-[u_\sigma]$), SSC_σ' ($=SSC_\sigma-[SSC_\sigma]$), and H' ($=H-[H]$) are the deviations of the u_σ, SSC_σ, and H from the tidal averages, respectively. The square brackets indicate the tidal averaging

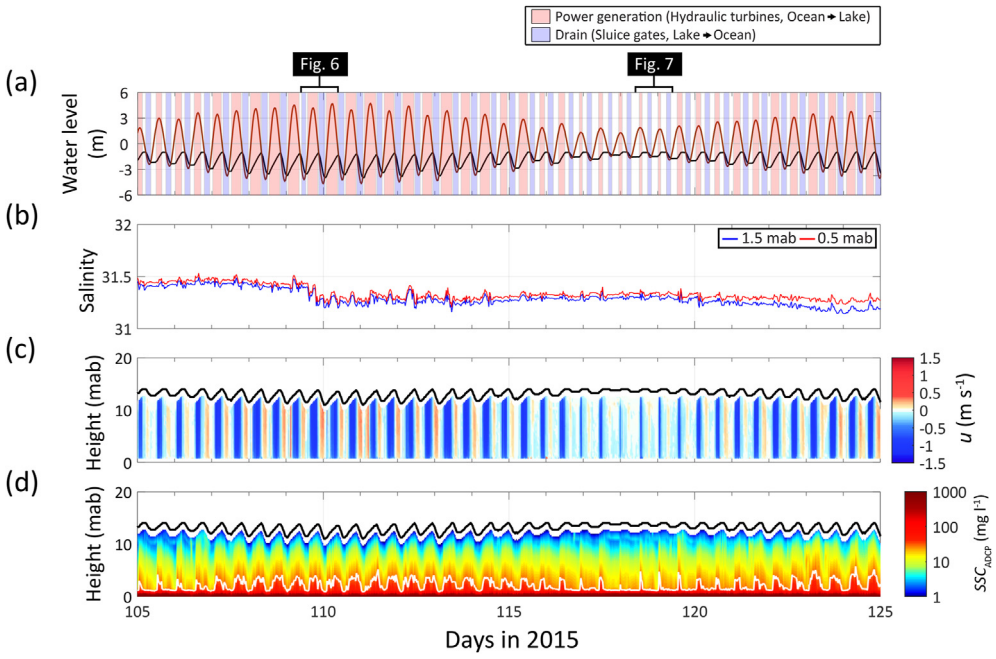


Fig. 5. Time series data for M3: (a) water level, (b) salinity at two levels, (c) along-channel velocity, and (d) SSC_{ADCP}. The brown and black lines in Fig. 5a indicate the water levels in the downstream and upstream, respectively. The thick black lines in Figs. 5c and d indicate the water height. The near-bed white line in Fig. 5d indicates 30 mg l^{-1}, used as the upper limit of bottom sediment suspension.

procedure. F_A represents the advective sediment flux by a residual current. F_D represents the sediment flux associated with time-varying tidal pumping, which includes contributions from the dispersive sediment flux.

4. Results

The water level variations in the downstream and upstream are shown in Fig. 5a. The tidal ranges were 8.7–8.9 m and 3.5–4.0 m during the spring tide (days 109–111) and neap tide (days 117–119), respectively. The water level in the upstream showed a pattern similar to the rise and drop of the tide. On the other hand, the water level varied between 2.28 and 2.85 m during the spring tide and between 0.37 and 0.85 m during the neap tide, which are relatively small compared to the tidal range in the downstream.

Sihwa TPP performed 38 flood generation cycles over the entire measurement period (red and blue shaded boxes in Fig. 5a). Power generation was operated for an average of 4.98 h. The longest and shortest durations of this phase were 7.3 h on days 111.11–111.41 and 1.7 h on days 119.01–119.08, respectively. The drain was operated for an average of 3.4 h. The longest and shortest durations of this phase were 4.1 h on days 109.87–110.04 and 2.3 h on days 117.67–117.77, respectively. The duration of the standby phase was less than 30 min during the spring tide and longer than 3 h during the neap tide. The periodic salinity peaks were observed during power generation phase, but the salinity variations were quite small (<0.4) (Fig. 5b). The salinities at 1.5 and 0.5 mab varied between 31.1 and 31.5, and the difference between 1.5 and 0.5 mab was about 0.05.

The current velocity and SSC at M3 were directly influenced by the jet. The current speed in u higher than 1.0 m s^{-1} always occurs during power generation phase (Fig. 5c). On the other hand, the current speed in u during other periods (except power generation) was less than 0.3 m s^{-1}. The u during the power generation was negative (SE-ward), whereas that during the drain was positive (NW-ward). The SSC_{ADCP} peaks were observed in both spring and neap tides, and they matched well with the increase in u during the power generation than that during the drain (Fig. 5d).

To examine the detail SSC variations, representative time windows were selected during the spring (days 109.40–110.40) and neap (days 118.4–119.4) tides (Fig. 5). The operation cycles of TPP were divided into two operation phases (T1 for power generation and T3 for drain) and two standby phases (T2 and T4).

4.1. SSC variations during the spring tide

During the spring tide between days 109.40–110.40 (Fig. 6), the durations of T1, T2, T3, and T4 were 6.5, 0.5, 4.1, and 1.0 h, respectively. The η_{diff} between downstream and upstream during T1 was four times greater than that during T3 (Fig. 6a). The maximum η_{diff} during T1 reached 6.40 m on day 109.70, whereas that during T3 reached 1.59 m on day 109.96.

The u exhibited opposite characteristics between T1 and T3 (Fig. 6b). During T1, u throughout the water column was always negative. An increase in u was observed 1 h after T1 began, and current speed in u at 1.0 mab ($u_{1.0\ mab}$) reached 0.7 m s^{-1} on day 109.77. During T3, u was mostly positive, as opposed to u during T1. The current speed in $u_{1.0\ mab}$ in T3 reached 0.2 m s^{-1} at 109.98 days, which was three times weaker than that in T1. The current speed in $u_{1.0\ mab}$ during T2 decreased from 0.5 to 0.2 m s^{-1}, whereas that during T4 increased from 0.1 to 0.2 m s^{-1}.

The SSC_{ADCP} at 1.0 mab ($SSC_{1.0\ mab}$) during T1 was twice higher than $SSC_{1.0\ mab}$ during T3 (Fig. 6c). During T1, the $SSC_{1.0\ mab}$ began to increase abruptly on day 109.60, and the highest $SSC_{1.0\ mab}$ reached 61.79 mg l^{-1} on day 109.79. When the $u_{1.0\ mab}$ turned to the deceleration stage of T1 (days 109.77–109.85), $SSC_{1.0\ mab}$ decreased rapidly to 30.71 mg l^{-1}. During T3, the $SSC_{1.0\ mab}$ decreased steadily with the lowest value of 23.09 mg l^{-1} on day 110.04. During T2, $u_{1.0\ mab}$ decreased to almost half of the velocity, but $SSC_{1.0\ mab}$ increased slightly to 37.66 mg l^{-1}. The $SSC_{1.0\ mab}$ was almost constant (~22.81 mg l^{-1}) during T4.

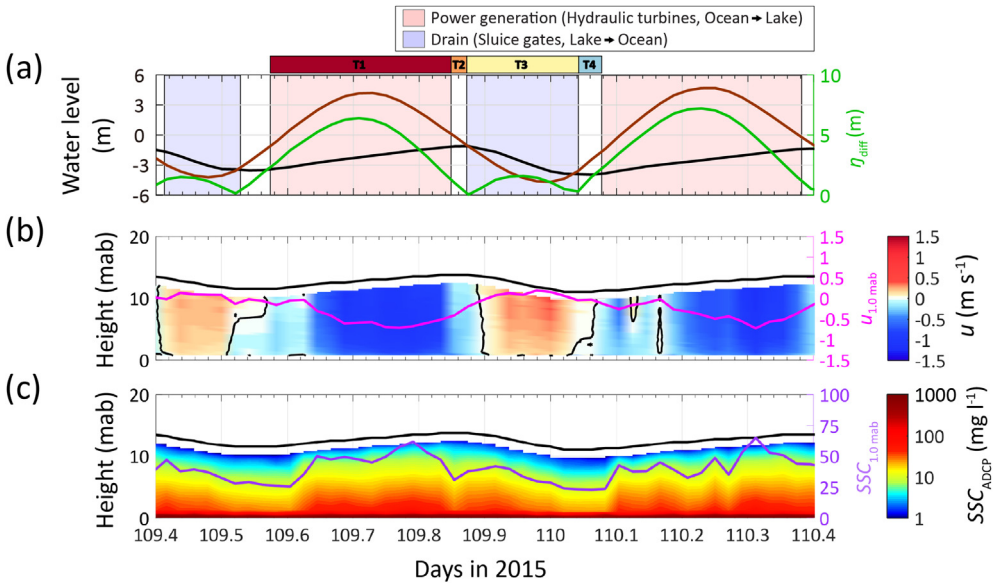


Fig. 6. Hydrodynamics and sediment dynamics for M3 during the spring tide (for the selected time window, see Fig. 5): (a) water level, (b) along-channel velocity, and (c) SSC_{ADCP}. The brown and black lines in Fig. 6a indicate the water levels in the downstream and the upstream, respectively. The green line is the water head difference between the downstream and upstream. The thick and thin black lines indicate the water height (Figs. 6b and c) and zero velocity (Fig. 6b), respectively. The pink line in Fig. 6b and purple line in Fig. 6c are the along-channel velocity and SSC_{ADCP} at 1.0 mab, respectively.

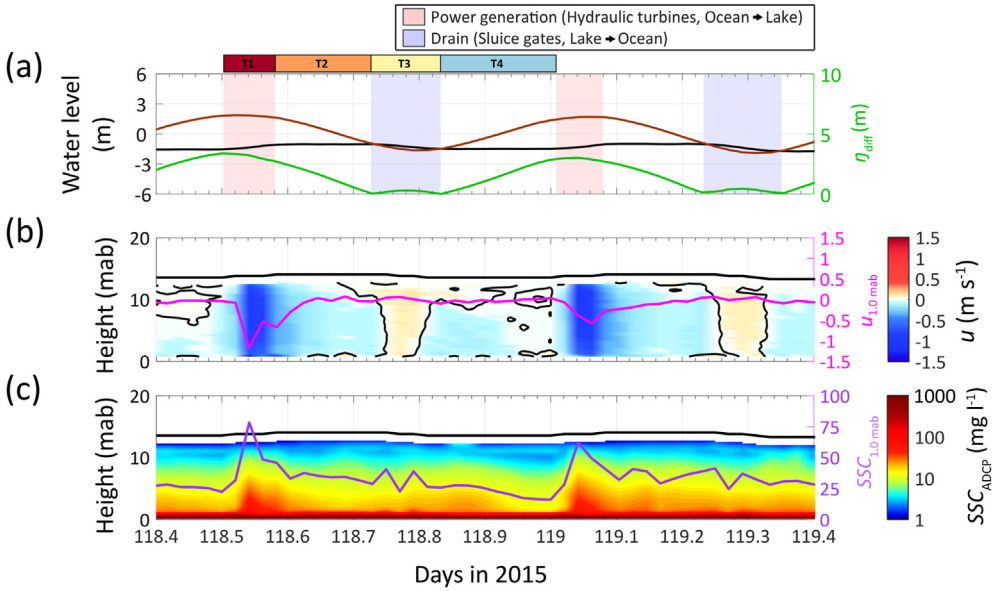


Fig. 7. Hydrodynamics and sediment dynamics for M3 during the neap tide (for the selected time window, see Fig. 5): (a) water level, (b) along-channel velocity, and (c) SSC_{ADCP}. The brown and black lines in Fig. 7a indicate the water levels downstream and upstream, respectively. The green line is the water head difference between downstream and the upstream. The thick and thin black lines indicate the water height (Figs. 7b and c) and zero velocity (Fig. 7b), respectively. The pink line in Fig. 7b and purple line in Fig. 7c are the along-channel velocity and SSC_{ADCP} at 1.0 mab, respectively.

4.2. SSC variations during the neap tide

During the neap tide between days 118.40–119.40 (Fig. 7), the durations of T1, T2, T3, and T4 were 1.9, 3.6, 2.9, and 4.3 h, respectively, with the standby phases lasting two times longer than the operation phases. The water level in the upstream area varied between −1.6 m and −1.0 m (Fig. 7a). The maximum η_{diff} during T1 and T3 reached 3.38 m on day 118.50 and 0.30 m on day 118.79. Similar to the profiles of u during the spring tide, those of u during the neap tide showed positive and negative between T1 and T3 (Fig. 7b). A remarkable $u_{1.0\ mab}$ was observed only in T1. During this period, the current speed in $u_{1.0\ mab}$ reached 1.2 m s^{-1}. In contrast, the current speed in $u_{1.0\ mab}$ in T2 sharply decreased, and $u_{1.0\ mab}$ during T2–T4 was almost constant between −0.1 and 0.1 m s^{-1}.

The $SSC_{1.0\ mab}$ peaks in T1 and relatively small $SSC_{1.0\ mab}$ peaks in T3 were observed during the neap tide (Fig. 7c). At the same time, as T1 began, an increase in $SSC_{1.0\ mab}$ appeared and the highest $SSC_{1.0\ mab}$ reached 78.28 mg l^{-1} on day 118.54. This coincided with the sharp increase in $u_{1.0\ mab}$ for 1 h of T1. During T3, the $SSC_{1.0\ mab}$ peaks of 40.35 mg l^{-1} and 38.62 mg l^{-1} were found on days 118.75 and 118.79, respectively. During T2 and T4, however, the $SSC_{1.0\ mab}$ tended to decrease steadily, and the lowest $SSC_{1.0\ mab}$ of T2 and T4

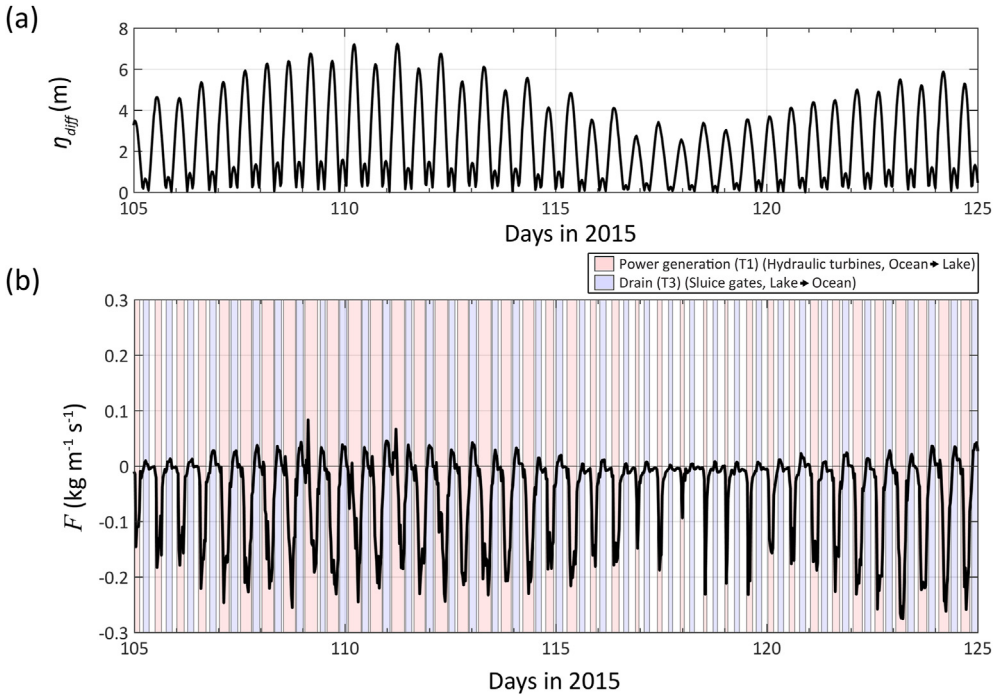


Fig. 8. Time series of (a) water head difference (η_{diff}) between the downstream and upstream and (b) the instantaneous sediment flux (F) at M3. The positive and negative F in Fig. 8b indicate the northwest- and southeast-ward fluxes, respectively.

were 28.53 and 15.82 mg l^{-1}, respectively.

4.3. Instantaneous sediment flux at M3

The F varied on the spring-neap cycle with higher fluxes observed on the spring tides (Fig. 8). F was mostly oriented positive during T3 (drain) and strongly negative (into the lake) during T1 (power generation). The increment in F higher than 0.1 kg m^{-1} s^{-1} was only observed during T1. The negative F during T1 reached −0.27 kg m^{-1} s^{-1} on day 123.21, whereas that during T3 reached 0.08 kg m^{-1} s^{-1} on day 109.12.

The discharge through the sluice gates with (Q_t) and without the hydraulic turbine (Q_s) is a key controlling factor determining the F around the TPP [13,39,40]. Bae et al. [17] presented the Q–η_{diff} relationships associated with four operation modes of T1 and T3 (Table 2) (see the bright red lines in Figs. 9a and b). As mentioned in Section 2, the Q_t in T1 increased in response to η_{diff} with a maximum of 474.4 m^3 s^{-1} at η_{diff} of 5.64 m, and it began to decrease at η_{diff} = 5.64 m due to generator efficiency. The curves of Q_s in T3 showed a logarithmic increase in response to η_{diff}, and maximum Q_s reached 1283.3 m^3 s^{-1} at 1.6 m.

The F variations at M3 are rarely related to the $Q_{t,s}$–η_{diff} variations. Fig. 9 shows the relationships between F and $Q_{t,s}$–η_{diff} during T1 and T3. For T1 (Figs. 9a and c), the R^2 of 0.55 between F and Q_t was related to the error during modes 2 and 3. The discharge in mode 1 was not performed through the hydraulic turbines, and then there were no F and η_{diff} results. The F variations in mode 2 were small with a standard deviation of 0.03 kg m^{-1} s^{-1} compared to the increase in η_{diff} because there was no suspension of bed sediment (e.g., days 109.58–109.62 and 109.80–109.84 in Fig. 6c). During the mode 3, the standard deviation in F reached a maximum of 0.05 kg m^{-1} s^{-1} in response to Q_t and η_{diff}, but the still low correlation ($R^2 < 0.3$) with the increase in F was due to low SSC variations (<10 mg l^{-1} in Fig. 6c). On the other hand, the error during mode 4 was moderate with a maximum standard deviation of 0.10 kg m^{-1} s^{-1}, resulting in a relatively high correlation of 0.6.

For T3 (Figs. 9b and d), the R^2 of 0.59 between F and Q_s was related to the error during modes 1–3. The standard deviation in mode 1 reached a maximum of 0.01 kg m^{-1} s^{-1} and the error from the regression line increased. The negative F in mode 1 still occurred with a decrease in SSC due to the short standby time (<0.5 h), resulting in the R^2 of 0.39 between F and Q_s–η_{diff}. During

Table 2
Q–η_{diff} relationship for the operation modes of T1 and T3 [17]. The Q_t and Q_s indicate the intensity of the discharge through the sluice gates with and without the hydraulic turbines, respectively.

Operation mode	Q– η_{diff} relationships
Power generation phase (T1)	
Mode-1 ($0 < \eta_{diff} < 1.07$)	$Q_t = 0$
Mode-2 ($1.07 \le \eta_{diff} < 1.95$)	$Q_t = 150.433 \times \eta_{diff} + 113.248179$
Mode-3 ($1.95 \le \eta_{diff} < 5.69$)	$Q_t = 18.1077 \times \eta_{diff} + 371.3606$
Mode-4 ($5.69 \le \eta_{diff} < 7.43$)	$Q_t = 1767.8881 - 346.5186 \times \eta_{diff} + 20.9571 \times \eta_{diff}^2$
Drain phase (T3)	
Mode-1 ($0 < \eta_{diff} < 0.05$)	$Q_s = 800 \times \eta_{diff} + 839 \times \eta_{diff}^{0.3855}$
Mode-2 ($0.05 \le \eta_{diff} < 0.1$)	$Q_s = 600 \times \eta_{diff} + 10 + 839 \times \eta_{diff}^{0.3855}$
Mode-3 ($0.1 \le \eta_{diff} < 0.3$)	$Q_s = 250 \times \eta_{diff} + 45 + 839 \times \eta_{diff}^{0.3855}$
Mode-4 ($0.3 \le \eta_{diff} < 1.6$)	$Q_s = 59.56939963 + 231.1052218 \times \eta_{diff} - 94.501852 \times \eta_{diff}^2 + 26.29460961 \times \eta_{diff}^3 - 2.754795024 \times \eta_{diff}^4 + 839 \times \eta_{diff}^{0.3855}$

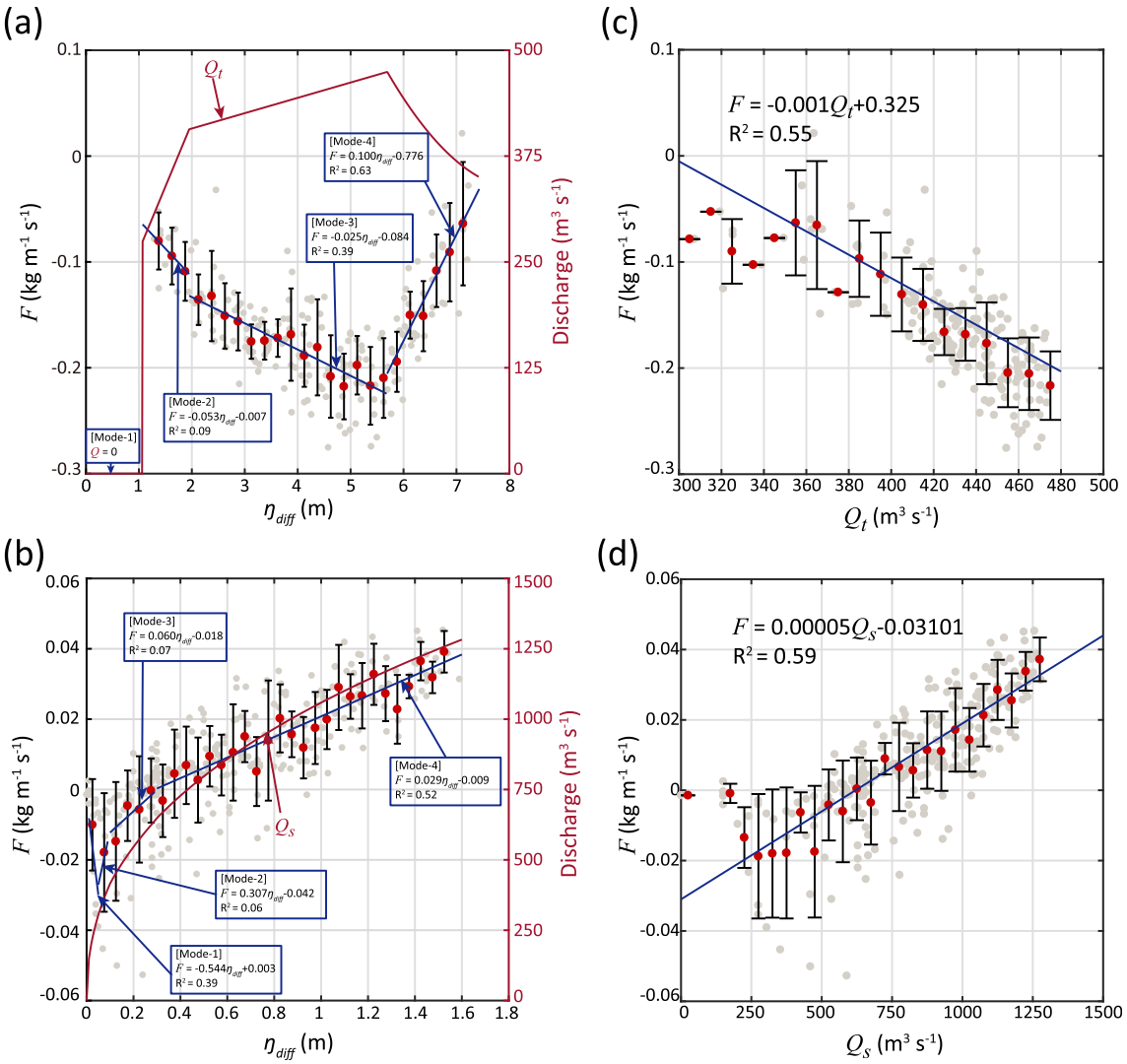


Fig. 9. Relationships between the instantaneous sediment flux (F), the water head difference (η_{diff}), and the discharges the sluice gates with (Q_t) and without the hydraulic turbine (Q_s) (a, c) during the T1 and (b, d) T3 phases. The dark blue lines indicate the linear regression between F, η_{diff}, and discharge (grey circles). The Q_t and Q_s were calculated using the orifice equation suggested in Bae et al. [17] (bright red lines in Figs. 9a and b). The black lines indicate the errorbar (standard deviation of the mean) in F, and the red circles are the average of F.

modes 2 and 3, the increase in Q_s—η_{diff} was not related to F ($R^2 < 0.1$) because the SSC decreased as F turned from negative to positive. These correlation results suggest that both Q_t and Q_s at the TPP gates have a weak effect of less than 60% on sediment influx at M3. Further discussion on the source of suspended sediment will be given in Section 5.

4.4. Residual sediment fluxes

The mechanisms and pathways of sediment transport can be explained by the subtidal signals (residual) of F [41–44]. Although tidal propagation has been blocked artificially by the seawall, tidal variations in the upstream were still observed at the upstream area due to periodic discharge. To distinguish the residual and tidal components, the spectral analysis was applied to the time series of the $SSC_{1.0\ mab}$, $u_{1.0\ mab}$, water level, and F. The selected time interval of each time series was 30 min to match with the interval of SSC derived from ADCP. The power spectral density of each time series was calculated using the Welch method [45] with 95% confidence intervals. A Hamming window with half-window overlaps was used. The length of the Hamming window was 64 h, yielding 15 degrees of freedom.

The spectral peaks for $SSC_{1.0\ mab}$, $u_{1.0\ mab}$, water level, and F were dominant at the semi-diurnal frequencies (M_2 and S_2) and overtide frequencies (M_4, M_6, and M_8) (Fig. 10). The presence of these tidal constituents in the water level, current velocity, SSC, and F indicated a strong potential for distortion and asymmetry of sediment transport associated with tidal forcing [46]. The residual components for $u_{1.0\ mab}$ and $SSC_{1.0\ mab}$ consist of long-period component longer than 48 h and indicate the mean flow and mean SSC over the tidal cycles.

The residual components in depth-averaged along-channel velocity ($\overline{u}$) and depth-averaged SSC_{ADCP} ($\overline{SSC}_{ADCP}$) are shown in Figs. 11b and c. The residual $\overline{u}$ was always negative (into the lake) and varied between −0.34 m s^{-1} and −0.10 m s^{-1}. The residual $\overline{SSC}_{ADCP}$ had a distinct spring-neap variation. The maximum residual $\overline{SSC}_{ADCP}$ reached 16.24 mg l^{-1} on day 112.0 during the spring tide, and reached 10.31 mg l^{-1} on day 118.1 during the neap tide.

F_T was always negative (into the lake) over the entire observation period, and showed spring-neap variations (Fig. 11d). The

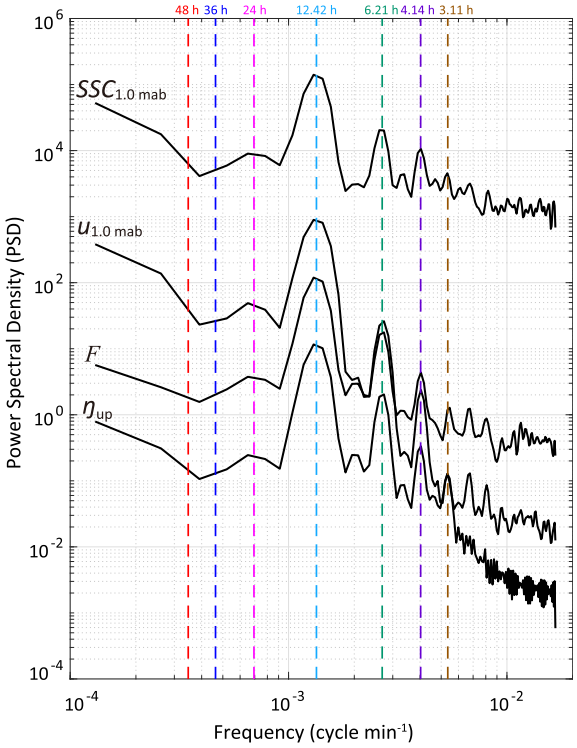


Fig. 10. Power spectral density (PSD) of water level in the upstream (η_{up}), suspended sediment concentration at 1.0 m above the bottom (mab) ($SSC_{1.0\ mab}$), instantaneous sediment flux (F), and along-channel velocity at 1.0 mab ($u_{1.0\ mab}$) at M3. Respective units of PSD are m^2 min for η_{up}, mg^2 l^{-2} min for $SSC_{1.0\ mab}$, kg^2 m^{-2} s^{-2} min for F, and m^2 s^{-2} min for $u_{1.0\ mab}$.

decomposition of F_T revealed the F_A induced by the product of residual flow and residual SSC to be the primary mechanism of a negative F_T (70–90% of F_T). F_D associated with time-varying tidal pumping was also negative, but F_D was much smaller than F_A. F_D was relatively constant over the spring and neap tide cycles. As F_T decreased during the neap tide, the relative contribution of F_D increased slightly. The inflow of sediment into the lake was dominated by the increased mean flow due to the discharge rather than natural asymmetry in the tidal currents.

5. Discussion

The most prominent result obtained in this study was that increment in F higher than 0.1 kg m^{-1} s^{-1} was skewed during T1, which was associated with the sediment influx into the upstream area observed in the jet-flow [47,48]. These processes affect the sediment budget of the semi-closed upstream. To explain the sediment accumulation, the depth-integrated cumulative sediment flux over the observation period (P) was calculated as follows:

$$\dot{F}_{T,A,D} = \int_0^P F_{T,A,D}\,dt, \tag{5}$$

where the subscripts (T, A, and D) indicate the total, mean advective, and the tidal dispersive components. Over 18 day mooring period, 78.28 tons m^{-1} of sediment was delivered into the lake (Fig. 11e). The $\dot{F}_T$ was always negative at about 30.19 and 11.49 tons m^{-1} over the spring (days 108–114) and neap tides (days 116–121), respectively. $\dot{F}_T$ is determined almost entirely by $\dot{F}_A$. 64.74 tons m^{-1} of sediment from $\dot{F}_A$ and 13.5 tons m^{-1} of sediment from $\dot{F}_D$ were delivered to the inside of the upstream area. Therefore, the sediment budget in the upstream tends to increase due to the mean advective sediment flux associated with the discharge.

The source of $\dot{F}_A$ was attributed to more local resuspension at M3 than by sediment inflow through the turbine gates of Sihwa TPP. The bed shear stress around the TPP can be magnified markedly by the strong near-bed flow induced by the submerged structure of the turbine gate [49]. In this study, the current speed at 1.0 mab showed a good linear relationship with SSC_{ADCP} at 1.0 mab for the T1 ($R^2 = 0.71$) (Fig. 12). In addition, the relationship between the Q–η_{diff} at the TPP gates and the increase in F during T1 were low ($R^2 < 0.6$) (Figs. 9a and c). These results mean that the high SSC (>30 mg l^{-1} in Fig. 5d) during power generation is caused by the resuspension of bottom sediment rather than by the sediment supply from the downstream region through the TPP gates.

As mentioned above, $\dot{F}_T$ at M3 was always negative (into the lake), which means the accumulation of sediment in the upstream. If the negative $\dot{F}_T$ is maintained continuously, the depth of the upstream has to become shallower. The sediment should be exported out of the upstream to balance it. A possible explanation for the outflux mechanism of sediment might be a complementary flow along both side channels during T3. However, these outfluxes alongside the channels were difficult to address directly because only the discharge data along the main passage are available. According to Blevins [50], the influence region of jet-flow decreases with increasing distance from the outlet of TPP, and the rotational flow is formed by the increase in horizontal velocity shear. At the reservoirs, the muddy flow induced by the rotational flow affects the outflux of sediment in the central region [51].

The 3-D hydrodynamic model, Finite Volume Community Ocean Model (FVCOM), was applied to Lake Sihwa to study the change in seawater circulations due to operation of Sihwa TPP [19]. The model results for residual flow clearly show that the seawater was circulated with the dipole vortex. The discharge creates the residual jet-flow structure in main passage of discharge. In addition, the dipole vortex induced a flow along the Sihwa tide embankment, resulting in a seawater flux converging on the jet-flow. Based on these model results for residual flow, the dramatic net sediment transport at the main passage of jet-flow suggests that suspended sediments were steadily transported into the lake. Most of suspended sediments introduced with the jet-flow will be isolated due to a dipole vortex. Therefore, the long-term sediment accumulation within Lake Sihwa is likely to be sustained by the operation of TPP.

Assessing the impacts of various TPP types on the sedimentary processes is a difficult and complex task [52]. The unbalanced sediment transport induced by the tidal power generation may be found not only in the flood generation type but also in the ebb and two-way generation types. Since more projects related to tidal power generation will be proposed in the near future, the mechanisms of sediment transport presented in this study can be a new guideline for an evaluation of sedimentary environments. We also expect to address problems such as flooding of rivers, dredging, and sediment contamination by understanding the sediment transport in response to the power generation.

6. Conclusions

An in-situ mooring study was conducted to understand the disturbance in sediment dynamics by the operation of Sihwa TPP. The following conclusions were drawn from this study:

(1) A $SSC_{1.0\ mab}$ peak at M3 was always observed in T1 over the spring and neap tidal cycles due to the opposite characteristics of $u_{1.0\ mab}$ between the power generation (T1) and drain

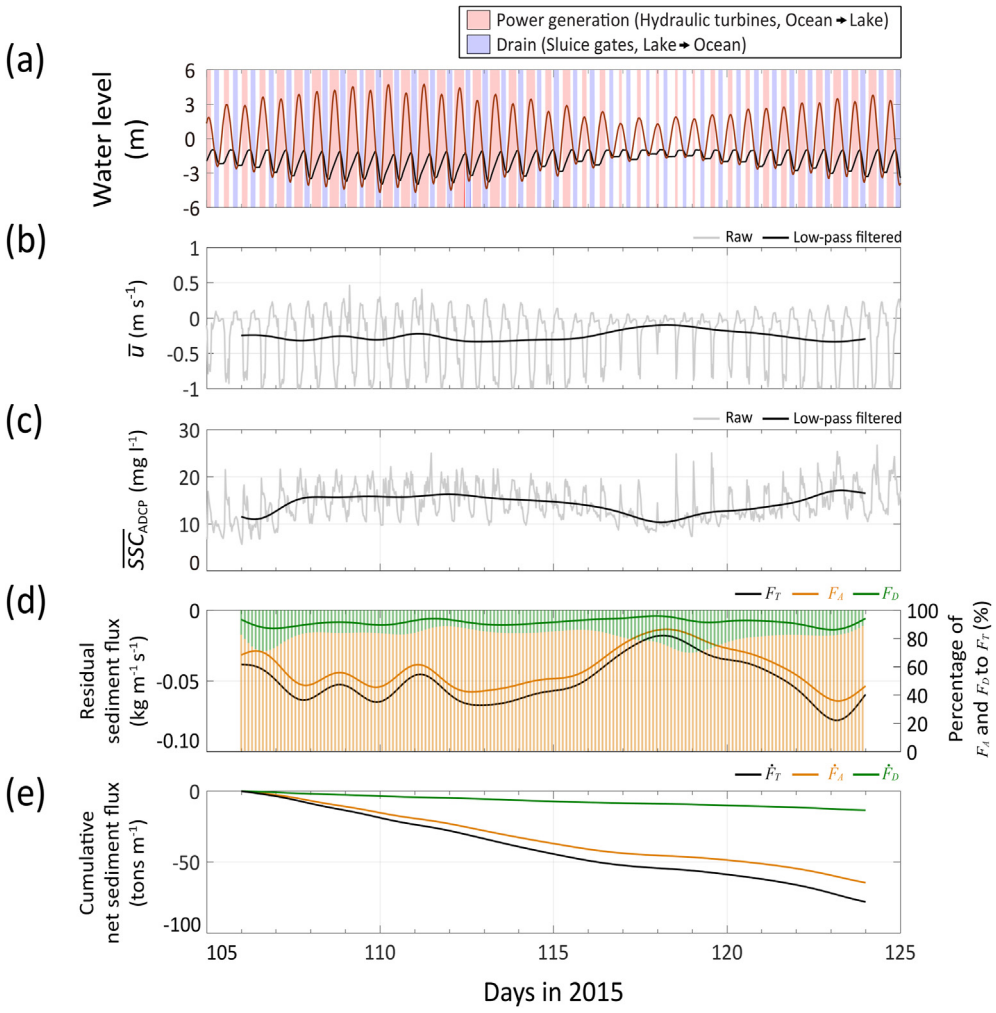


Fig. 11. Residual components from mooring M3 in 2015: (a) water level, (b) depth-averaged along-channel velocity ($\bar{u}$), (c) depth-averaged SSC_{ADCP} ($\overline{SSC}_{ADCP}$), (d) residual sediment flux, and (e) cumulative net sediment flux. The brown and black lines in Fig. 11a indicate the water levels in the downstream and upstream, respectively. The F_T, F_A, and F_D in Figs. 11d and e are the total, mean advective, and dispersive sediment flux, respectively. The light orange and light green stacked bar graphs in Fig. 11d are the contribution percentage of F_A and F_D, respectively, on F_T.

(T3) phases. An increase in $SSC_{1.0\ mab}$ with strong SE-ward $u_{1.0\ mab}$ (>1 m s^{-1}) was observed during T1, whereas the decrease in $SSC_{1.0\ mab}$ with a relatively weak NW-ward $u_{1.0\ mab}$ (<0.4 m s^{-1}) was observed during T3.

(2) The high SSC (>30 mg l^{-1}) during power generation was caused by the resuspension of near-bed sediment rather than by the sediment supply from the downstream through the gates of TPP. The relationship between the curve of Q–η_{diff} at the gates of TPP and the increase in F during T1 was relatively low ($R^2 < 0.63$). On the other hand, the current speed in $u_{1.0\ mab}$ at M3 showed a good linear regression with $SSC_{1.0\ mab}$ for T1 ($R^2 = 0.71$).

(3) The inflow of sediment into the lake was controlled by the increased mean flow due to artificial discharge rather than natural asymmetry in the tidal currents. The F_A induced by the product of residual velocity and SSC was 70–90% of F_T over an entire measurement period. On the other hand, the contribution of F_D associated with time-varying tidal pumping was 10–30%, which is relatively low compared to F_A.

(4) Based on the fact that 78.28 tons m^{-1} of sediment at M3 was delivered to the lake over 18 day mooring period, the annual sediment flux is roughly estimated to be about 1.59 × 10^3 tons m^{-1}. Since the maximum influx of sediment during power generation phase occurred within the η_{diff} of 4–6 m, the reduction in discharge rate can be a possible measure for solving the sediment accumulation within Lake Sihwa.

CRediT authorship contribution statement

J.W. Kim: Conceptualization, Methodology, Investigation, Software, Writing – original draft, Writing – review & editing, Visualization. **H.K. Ha:** Supervision, Conceptualization, Methodology, Project administration, Writing – original draft, Writing – review & editing. **S.-B. Woo:** Investigation, Methodology, Conceptualization, Writing – original draft, Visualization. **M.-S. Kim:** Methodology, Conceptualization, Writing – original draft, Writing – review & editing, Visualization. **H.-K. Kwon:** Project administration, Writing – review & editing, Resources.

Declaration of competing interest

The authors declare that they have no known competing financial interests or personal relationships that could have appeared to influence the work reported in this paper.

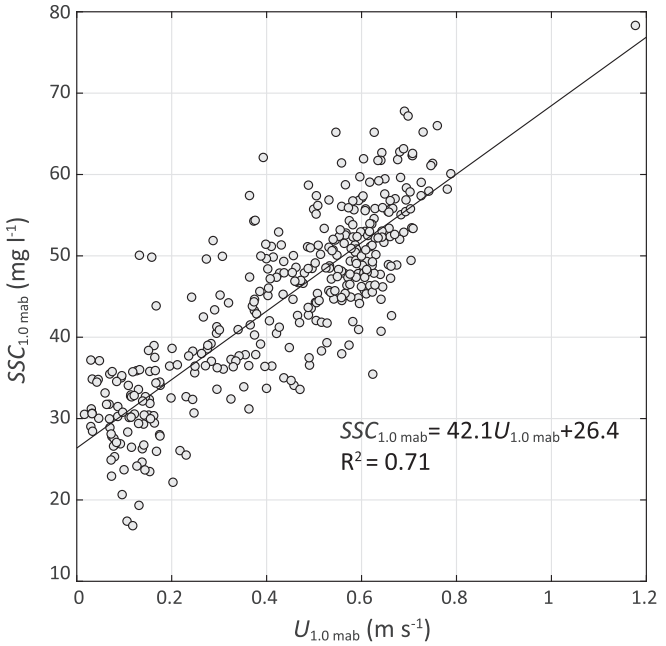


Fig. 12. Relationship between the SSC_{ADCP} ($SSC_{1.0\ mab}$) and the along-channel velocity ($U_{1.0\ mab}$) at 1.0 mab during the power generation (T1).

Acknowledgments

This research was a part of the project titled 'Gyeonggi Sea Grant Program' and 'Improvements of ocean prediction accuracy using numerical modeling and artificial intelligence technology', funded by the Ministry of Oceans and Fisheries, Korea. It was also supported by the National Research Foundation of Korea (NRF-2018R1D1A1A02085804).

References

[1] D.A. Jay, P.M. Orton, T. Chisholm, D.J. Wilson, A.M.V. Fain, Particle trapping in stratified estuaries: application to Observations, Estuar. Coast 30 (2007) 1106–1125, https://doi.org/10.1007/BF02841400.
[2] D.K. Young, D.C. Rhoads, Animal-sediment relations in Cape Cod Bay, Massachusetts I. A transect study, Mar. Biol. 11 (1971) 242–254, https://doi.org/10.1007/BF00401272.
[3] D.W. Pritchard, Salinity distribution and circulation in the Chesapeake Bay estuarine system, J. Mar. Res. 11 (1952) 106–123.
[4] G.P. Allen, J.C. Salomon, P. Bassoullet, Y. Du penhoat, C. de Grandpré, Effects of tides on mixing and suspended sediment transport in macrotidal estuaries, Sediment. Geol. 26 (1980) 69–90, https://doi.org/10.1016/0037-0738(80)90006-8.
[5] J.H. Gao, J. Jia, A.J. Kettnet, F. Xing, Y.P. Wang, X.N. Xu, Y. Yang, X.Q. Zou, S. Gao, S. Qi, F. Liao, Changes in water and sediment exchange between the Changjiang River and Poyang Lake under natural and anthropogenic conditions, China, Sci. Total Environ. 481 (2014) 542–553, https://doi.org/10.1016/j.scitotenv.2014.02.087.
[6] D.H. Schoellhamer, Anthropogenic sediment resuspension mechanisms in a shallow microtidal estuary, Estuar. Coast Shelf Sci. 43 (1996) 533–548, https://doi.org/10.1006/ecss.1996.0086.
[7] F. O'Rourke, F. Boyle, A. Reynolds, Tidal energy update 2009, Appl. Energy 87 (2010) 398–409, https://doi.org/10.1016/j.apenergy.2009.08.014.
[8] C. Baker, Tidal power, Energy Pol. 19 (1991) 792–797, https://doi.org/10.1016/0301-4215(91)90049-T.
[9] R.H. Charlier, Ocean alternative energy: the view from China–'Small is beautiful, Renew. Sustain. Energy Rev. 5 (4) (2000) 403–409, https://doi.org/10.1016/S1364-0321(01)00005-3.
[10] R.H. Charlier, Sustainable co-generation from the tides: a review, Renew. Sustain. Energy Rev. 7 (2003) 187–213, https://doi.org/10.1016/S1364-0321(02)00011-4.
[11] S.P. Neill, A. Angeloudis, P.E. Robins, I. Walkington, S.L. Ward, I. Masters, M.J. Lewis, M. Piano, A. Avdis, M.D. Piggott, G. Aggidis, P. Evans, T.A.A. Adcock, A. Zidonis, R. Ahmadian, R. Falconer, Tidal range energy resource and optimization–Past perspectives and future challenges, Renew. Energy 127 (2018) 763–778, https://doi.org/10.1016/j.renene.2018.05.007.
[12] R. Kirby, C. Retière, Comparing environmental effects of Rance and Severn barrages, Proc. Inst. Civ. Eng. Marit. Eng. 162 (2009) 11–26, https://doi.org/10.1680/maen.2009.162.1.11.
[13] R.A. Falconer, J. Xia, B. Lin, R. Ahmadian, The Severn Barrage and other tidal energy options: hydrodynamic and power output modeling, Sci. China Ser. E-Technol. Sci. 52 (2009) 3413–3424, https://doi.org/10.1007/s11431-009-0366-z.
[14] J. Wolf, I. Walkington, J. Holt, R. Burrows, Environmental impacts of tidal power schemes, Proc. Inst. Civ. Eng. Marit. Eng. 162 (2009) 165–177, https://doi.org/10.1680/maen.2009.162.4.165.
[15] M. Kadiri, R. Ahmadian, B. Bockelmann-Evans, W. Rauen, R. Falconer, A review of the potential water quality impacts of tidal renewable energy systems, Renew. Sustain. Energy Rev. 16 (2012) 329–341, https://doi.org/10.1016/j.rser.2011.07.160.
[16] D.C. Gordon Jr., Intertidal ecology and potential power impacts, Bay of Fundy, Canada, Bio, J. Linnean Soc. 51 (1994) 17–23, https://doi.org/10.1006/bijl.1994.1003.
[17] Y.H. Bae, K.O. Kim, B.H. Choi, Lake Sihwa tidal power plant project, Ocean Eng. 37 (2010) 454–463, https://doi.org/10.1016/j.oceaneng.2010.01.015.
[18] J.W. Kim, H.K. Ha, S.B. Woo, Dynamics of sediment disturbance by periodic artificial discharges from the world's largest tidal power plant, Estuar. Coast Shelf Sci. 190 (2017) 69–79, https://doi.org/10.1016/j.ecss.2017.03.029.
[19] J.W. Kim, Effects of Periodic Discharges from a Sihwa Tidal Power Plant on the Hydrodynamics and Sediment Transport, Ph.D. Dissertation, Inha University, Incheon, 2020, pp. 104–173.
[20] Y.H. Bae, B.I. Yoon, C.H. Seo, S.J. Park, K.-Y. Bang, H.-K. Kwon, S.-B. Woo, Residence time variation by operation of Sihwa tidal power plant in outer sea of Sihwa lake, J. Kor. Soc. Coast. Ocean Eng. 29 (5) (2017) 247–259, https://doi.org/10.9765/KSCOE.2017.29.5.247.
[21] Korea Water Resources Corporation (K-Water), Long-term observational study of the physical oceanographic changes by the tidal power plant Operation, in: Research and Development Report, 2017, p. 407.
[22] Y. Lee, J. Hur, K. Shin, Characterization and source identification of organic matter in view of land uses and heavy rainfall in the Lake Shihwa, Korea, Mar. Pollut. Bull. 84 (2014) 322–329, https://doi.org/10.1016/j.marpolbul.2014.04.033.
[23] J. Lee, K.T. Park, J.H. Lim, J.E. Yoon, I.N. Kim, Hypoxia in Korean coastal waters: a case study of the natural Jinhae Bay and artificial Shihwa Bay, Front. Mar. Sci. 5 (2018) 1–19, https://doi.org/10.3389/fmars.2018.00070.
[24] M.W. Han, Y.C. Park, The development of anoxia in the artificial lake Shihwa, Korea, as a consequence of intertidal reclamation, Mar. Pollut. Bull. 38 (1999) 1194–1199, https://doi.org/10.1016/S0025-326X(99)00161-7.
[25] C.H. Lee, B.Y. Lee, W.K. Chang, S. Hong, S.J. Song, J. Park, B.O. Kwon, J.S. Khim, Environmental and ecological effects of Lake Shihwa reclamation project in South Korea: a review, Ocean Coast Manag. 102 (2014) 545–558, https://doi.org/10.1016/j.ocecoaman.2013.12.018.
[26] S. Jeon, S. Hong, B.O. Kwon, J. Park, S.J. Song, J.P. Giesy, J.S. Khim, Assessment of potential biological activities and distributions of endocrine-disrupting chemicals in sediments of the west coast of South Korea, Chemosphere 168 (2017) 441–449, https://doi.org/10.1016/j.chemosphere.2016.10.089.
[27] Y. Lee, J. Hur, K. Shin, Characterization and source identification of organic matter in view of land uses and heavy rainfall in the Lake Shihwa, Korea, Mar. Pollut. Bull. 84 (2014) 322–329, https://doi.org/10.1016/j.marpolbul.2014.04.033.
[28] A. Angeloudis, R.A. Falconer, S. Bray, R. Ahmadian, Representation and operation of tidal energy impoundments in a coastal hydrodynamic model, Renew. Energy 99 (2016) 1103–1115, https://doi.org/10.1016/j.renene.2016.08.004.
[29] J. Xia, R.A. Falconer, B. Lin, Impact of different tidal renewable energy projects on the hydrodynamic processes in the Severn Estuary, UK, Ocean Model. 32 (2010) 86–104, https://doi.org/10.1016/j.ocemod.2009.11.002.
[30] Y.S. Kang, Y. Chae, H.R. Lee, Changes in sea water characteristics due to operation of Shihwa tidal power plant, J. Kor. Soc. Coast. Ocean Eng. 25 (4) (2013) 219–235, https://doi.org/10.9765/KSCOE.2013.25.4.219.
[31] K.L. Deines, Backscatter estimation using broadband acoustic Doppler current profilers, in: Proceedings of the 6th IEEE Working Conference on Current Measurement, San Diego, CA, 1999, pp. 249–253, https://doi.org/10.1109/CCM.1999.755249.
[32] H.K. Ha, J.P.-Y. Maa, K. Park, Y.H. Kim, Estimation of high-resolution sediment concentration profiles in bottom boundary layer using pulse-coherent acoustic Doppler current profilers, Mar. Geol. 279 (2011) 199–209, https://doi.org/10.1016/j.margeo.2010.11.002.
[33] F.H. Fisher, V.P. Simmons, Sound absorption in sea water, J. Acoust. Soc. Am. 62 (1977) 558, https://doi.org/10.1121/1.381574.
[34] S.D. Richards, A.D. Heathershaw, P.D. Thorne, The effect of suspended particulate matter on sound attenuation in seawater, J. Acoust. Soc. Am. 100 (1996) 1447–1450, https://doi.org/10.1121/1.415991.
[35] H.-B. Park, G.-H. Lee, Evaluation of ADCP backscatter inversion to suspended sediment concentration in Estuarine environments, Ocean Sci. J. 51 (1) (2016) 109–125, https://doi.org/10.1007/s12601-016-0010-3.
[36] S.N. Giddings, S.G. Monismith, D.A. Fong, M.T. Stacey, Using depth-normalized coordinates to examine mass transport residual circulation in estuaries with large tidal amplitude relative to the mean depth, J. Phys. Oceanogr. 44 (2014) 128–148, https://doi.org/10.1175/JPO-D-12-0201.1.
[37] W.R. Geyer, J.D. Woodruff, P. Traykovski, Sediment transport and trapping in the Hudson River estuary, Estuaries 24 (2001) 670–679, https://doi.org/

10.2307/1352875.
[38] C.K. Sommerfield, K.C. Wong, Mechanisms of sediment flux and turbidity maintenance in the Delaware Estuary, J. Geophys. Res. 116 (2011) 1–16, https://doi.org/10.1029/2010JC006462.
[39] N. Yates, I. Walkington, R. Burrows, J. Wolf, The energy gains realizable through pumping for tidal range energy schemes, Renew. Energy 58 (2013) 79–84, https://doi.org/10.1016/j.renene.2013.01.039.
[40] S.P. Neill, E.J. Litt, S.J. Couch, A.G. Davies, The impact of tidal stream turbines on large-scale sediment dynamics, Renew. Energy 34 (2009) 2803–2812, https://doi.org/10.1016/j.renene.2009.06.015.
[41] D. Bryant, K. Whilden, S. Socolofsky, K. Chang, Formation of tidal starting-jet vortices through idealized barotropic inlets with finite length, Environ. Fluid Mech. 12 (4) (2012) 301–319, https://doi.org/10.1007/s10652-012-9237-4.
[42] A. Valle-Levinson, X. Guo, Asymmetries in tidal flow over a Seto Inland Sea scour pit, J. Mar. Res. 67 (5) (2009) 619–635, https://doi.org/10.1357/002224009791218850.
[43] D.K. Ralston, J.C. Warner, W.R. Geyer, G.R. Wall, Sediment transport due to extreme events: the Hudson River estuary after tropical storms Irene and Lee, Geophys. Res. Lett. 40 (2013) 5451–5455, https://doi.org/10.1002/2013GL057906.
[44] M. Pritchard, M. Green, Trapping and episodic flushing of suspended sediment from a tidal river, Continent. Shelf Res. 143 (2017) 286–294, https://doi.org/10.1016/j.csr.2016.07.007.
[45] P. Welch, The use of fast fourier transform for the estimation of power spectra: a method based on time averaging over short, modified periodograms, IEEE Trans. Audio Electroacoust. 15 (2) (1967) 70–73.
[46] W. Gong, L. Jia, J. Shen, J. Liu, Sediment transport in response to changes in river discharge and tidal mixing in a funnel-shaped micro-tidal estuary, Continent. Shelf Res. 76 (2014) 89–107, https://doi.org/10.1016/j.csr.2014.01.006.
[47] Y.B. Broekema, R.J. Labeur, W.S.J. Uijttewaal, Observations and analysis of the horizontal structure of a tidal jet at Deep Scour Holes, J. Geophys. Res.-Earth 123 (2018) 3162–3189, https://doi.org/10.1029/2018JF004754.
[48] M.R. Boroomand, A.A.S. Neyshabouri, K. Aghajanloo, Numerical simulation of sediment transport and scouring by an offset jet, Can. J. Civ. Eng. 34 (10) (2007) 1267–1275, https://doi.org/10.1139/l07-050.
[49] P. Jetffcoate, P. Stansby, D. Apsley, Flow and bed-shear magnification downstream of a barrage with swirl generated in ducts by stators and rotors, J. Hydraul. Eng. 143 (2) (2016), https://doi.org/10.1061/(ASCE)HY.1943-7900.0001228, 06016023.
[50] R.D. Blevins, Applied Fluid Dynamics Handbook, first ed., Krieger, Malabar, Florida, 1984.
[51] A. Jenzer, G.J. Cesare, A. Schleiss, Sediment evacuation from reservoirs through intakes by jet-induced flow, J. Hydraul. Eng. 141 (2) (2015), https://doi.org/10.1061/(ASCE)HY.1943-7900.0000970, 04014078.
[52] Y. Wu, C. Xu, Y. Ke, K. Chen, H. Xu, Multi-criteria decision-making on assessment of proposed tidal barrage schemes in terms of environmental impacts, Mar. Pollut. Bull. 125 (2017) 271–281, https://doi.org/10.1016/j.marpolbul.2017.08.030.